Geophysical Journal International

Geophys. J. Int. (2016) **204,** 236–249 doi: 10.1093/gji/ggv446
GJI Seismology

Probabilistic waveform inversion for 22 earthquake moment tensors in Hungary: new constraints on the tectonic stress pattern inside the Pannonian basin

Zoltán Wéber

*Kövesligethy Radó Seismological Observatory, MTA CSFK GGI, H-*1112 *Budapest, Meredek u.* 18, *Hungary. E-mail: weber@seismology.hu*

Accepted 2015 October 13. Received 2015 September 23; in original form 2015 March 25

SUMMARY

We have successfully estimated the full moment tensors of 22 local earthquakes with local magnitude ranging from 1.2 to 4.8 that occurred in the Hungarian part of the Pannonian basin between 1995 and 2014. We used a probabilistic waveform inversion procedure that takes into account the effects of the random noise contained in the seismograms, the uncertainty of the hypocentre determined from arrival times and the inaccurate knowledge of the velocity structure, while estimating the error affecting the derived focal parameters. The applied probabilistic approach maps the posterior probability density functions (PPDFs) for both the hypocentral coordinates and the moment tensor components. The final estimates are given by the maximum likelihood points of the PPDFs, while solution uncertainties are presented by histogram plots. The estimated uncertainties in the moment tensor components are plotted on the focal sphere in such a way, that the significance of the double couple (DC), the compensated linear vector dipole (CLVD) and the isotropic (ISO) parts of the source can be assessed. We have shown that the applied waveform inversion method is equally suitable to recover the source mechanism for low-magnitude events using short-period local waveforms as well as for moderate-size earthquakes using long-period seismograms. The non-DC components of the retrieved focal mechanisms are statistically insignificant for all the analysed earthquakes. The negligible amount of the ISO component implies the tectonic nature of the investigated events. The moment tensor solutions reported by other agencies for five of the $M_L > 4$ earthquakes studied in this paper are very similar to those calculated by the applied waveform inversion algorithm. We have found only strike-slip and thrust faulting events, giving further support to the hypothesis that the Pannonian basin is currently experiencing a compressional regime of deformation. The orientations of the obtained focal mechanisms are in good agreement with the main stress pattern published for the Pannonian region. The azimuth of the subhorizontal *P* principal axis varies from about NNE-SSW in SW Hungary through NE-SW well inside the basin to around E-W in the NE part of the country. Most of the analysed earthquakes occurred on faults or subfaults differently oriented than the main fault system.

Key words: Time-series analysis; Inverse theory; Probability distributions; Earthquake source observations; Neotectonics.

1 INTRODUCTION

In Hungary (the central part of the Pannonian basin), seismic activity can be characterised as moderate. The seismicity pattern shows that earthquakes are restricted to the upper part of the crust and the epicentres are distributed all around the country. Therefore, identification of active fault planes is generally a difficult issue in this region. However, there are certain areas where seismicity is higher and where significant, destructive earthquakes with magnitude $M > 5$ occurred in the last centuries (Zsíros 2000). Statistical studies show that four to five *M* 2.5–3.5 earthquakes can be expected every year in the country, which can be felt near the epicentre, but cause no damage (Tóth *et al.* 2002). Earthquakes causing light damages occur every 15–20 yr, whereas stronger, more damaging (*M* 5.5–6) quakes happen about every 40–50 yr. Moreover, about 100 small-magnitude local events are detected instrumentally every year.

In areas of low-to-moderate seismicity, the small-magnitude local earthquakes provide the only key to determine fault parameters and small-scale tectonic structure. The focal mechanisms of small

($M < 4$) events can be used to infer the structure and kinematics of faults at depth and to constrain the crustal stress field in which the earthquakes occur. It is therefore important to determine mechanisms for small events as accurately as possible. These mechanisms are most often found using *P*-wave first-motion polarities recorded at local seismic stations. Each observed *P* arrival is mapped to the orientation at which the ray left the focal sphere and nodal planes are fit to the set of observations (e.g. Reasenberg & Oppenheimer 1985; Hardebeck & Shearer 2002). Since only the binary up or down of the first motions counts in these methods, a dense sampling of the focal sphere is required to form a reliable solution. For many small earthquakes, the lack of sufficient first-motion observations causes large uncertainties in their focal mechanisms.

With the widespread growth of broad-band instruments, long-period (>5 s) waveform inversion techniques have been developed and proven effective in retrieving accurate source mechanisms of earthquakes with $M \sim 4$ and greater (e.g. Saikia & Herrmann 1985; Dreger & Helmberger 1993; Zhao & Helmberger 1994; Zhu & Helmberger 1996; Liu *et al.* 2004; Sokos & Zahradnik 2008; Zahradnik & Sokos 2014). Since seismic waveforms contain much more information about the source than the first-motion polarities alone, even sparse data sets suffice for the task. The same strategy, however, can hardly be applied to smaller events, because of the poor signal-to-noise ratio (SNR) at long periods. Low-magnitude local events have to be analysed at much higher frequencies (>0.5 Hz). Several procedures have been proposed to estimate the focal mechanism of low-magnitude earthquakes by using high-frequency seismograms recorded at local stations (e.g. Šílený *et al.* 1992; Mao *et al.* 1994; Panza & Sarao 2000; Sarao *et al.* 2001; Vavryčuk & Kühn 2012).

Recently, probabilistic point-source inversion schemes have been published for both local (Debski 2008) and global (Stähler & Sigloch 2014) events. Wéber (2005, 2006, 2009) has also developed a Bayesian waveform inversion procedure in order to retrieve the hypocentral locations and source mechanisms (full moment tensors) of local earthquakes. The inversion of high-frequency local waveforms is rather sensitive to several types of errors, such as imperfect location of the hypocentre, mismodelling of velocity inhomogeneities, neglect of anisotropy of the crust, etc. However, according to our experience, our algorithm is usually able to reliably estimate the focal mechanisms of local events with moment magnitude $M_w \sim 2$ or greater, good SNR and reasonable azimuthal station coverage. The procedure has successfully been applied for estimating the focal mechanism of the 2011 January 29 M_L 4.5 Oroszlány (Hungary) earthquake and its four aftershocks (Wéber & Süle 2014).

In this paper, we study the source mechanisms (full moment tensors) of 22 manually selected earthquakes that occurred in Hungary in the last two decades. For events with local magnitude $M_L > 4$ we used long-period waveforms, whereas for smaller events we utilised short-period seismograms in the inversion procedure. We also discuss the quality and reliability of the results and compare the retrieved focal mechanisms to the main stress pattern published for the epicentral regions.

After a short overview of the tectonic setting of the Pannonian basin and a description of data selection and processing, we present the waveform inversion method that we applied on the available broad-band and short-period records. The moment tensor solutions that we obtained are then discussed, with some preliminary tectonic implications. Here we would like to emphasise that our provisional focal mechanism catalogue is the first one that contains full moment tensors for local earthquakes in Hungary. In fact, to the best of our knowledge, probabilistic source mechanism solutions for such a large number of earthquakes have never been published before.

2 TECTONIC SETTING OF THE PANNONIAN BASIN

The Pannonian basin is situated within the Alpine, Carpathian and Dinaric mountain belts. Recent studies have shown that the present structural layout of the Pannonian basin can be considered as a result of complex kinematic and dynamic processes that took place since the Neogene, triggered by the continental collision between Europe and several continental fragments to the south (e.g. Horváth 1993; Neubauer *et al.* 1995; Decker *et al.* 1998; Bada *et al.* 1999). Subduction of the European foreland and associated rollback of the subducted slab caused lithospheric extension and asthenospheric updoming during the Middle Miocene while discrete basins opened up due to the extension (Horváth 1993; Bada *et al.* 2001). In the Late Miocene, the asthenospheric dome cooled down leading to the subsidence of the whole basin system. In the latest Pliocene and Quaternary, the movement of the Adriatic microplate led to the end of the subsidence and to the structural inversion of the Pannonian basin (Bada *et al.* 2007).

Geophysical features such as an updoming of the mantle, a thinned lower crust and a strong geothermal anomaly are all characteristic to the basin. Mostly due to the high Moho temperature, the mean *P*-wave velocity in the uppermost mantle is 7.9 km s^{-1}, substantially lower than the average continental P_n velocity of 8.1 km s^{-1} (Wéber 2002; Gráczer & Wéber 2012). The crust is rather thick (>40 km) in the mountain ranges around the Pannonian basin, whereas the basin itself is characterised by thin crust, ranging from 22.5 to 30 km, where the 30 km depth isoline encircles the whole basin (Horváth 1993). The lithosphere also has smaller thickness than the continental average. Several geophysical studies suggest that the lithosphere under the basin is thinner than 80 km (e.g. Babuska *et al.* 1987; Posgay *et al.* 1995). The several types of deformation having taken place in the Pannonian basin are partly hidden by a thick sequence of sedimentary rocks of Neogene–Quaternary age. The average thickness of the sedimentary layers is about 3 km with a maximum value of about 8 km (Kilényi *et al.* 1991).

The recent tectonic activity of the Pannonian region is basically determined by the counter-clockwise rotation and north-northeast drift of the Adriatic microplate relative to Europe. In addition, lateral extrusion of crustal flakes from the axis of the Alpine orogen has a significant role in the stress pattern, particularly in the western Pannonian basin (Bada *et al.* 2007). Due to the convergence between Adria and the Alps and the Dinarides, the lithosphere in the Pannonian basin and its vicinity is subjected to compressional tectonic stresses. As a result, strike-slip to compressive faulting is observed well inside the basin. The nearly complete absence of normal faulting in the area suggests that in the Pannonian basin structural inversion is in progress (Bada *et al.* 1999, 2007; Gerner *et al.* 1999; Fodor *et al.* 2005).

From the edges of Adria toward the basin centre, the stress regime gradually changes from pure compression to a strike-slip type stress field. Neotectonic structures in the Pannonian region are largely controlled by the reactivation of pre-existing shear zones. Accordingly, reverse faulting in the basement leads to folding of the overlying strata in the west. Toward the east, the style of deformation becomes strike-slip faulting (Fodor *et al.* 2005; Bada *et al.* 2007).

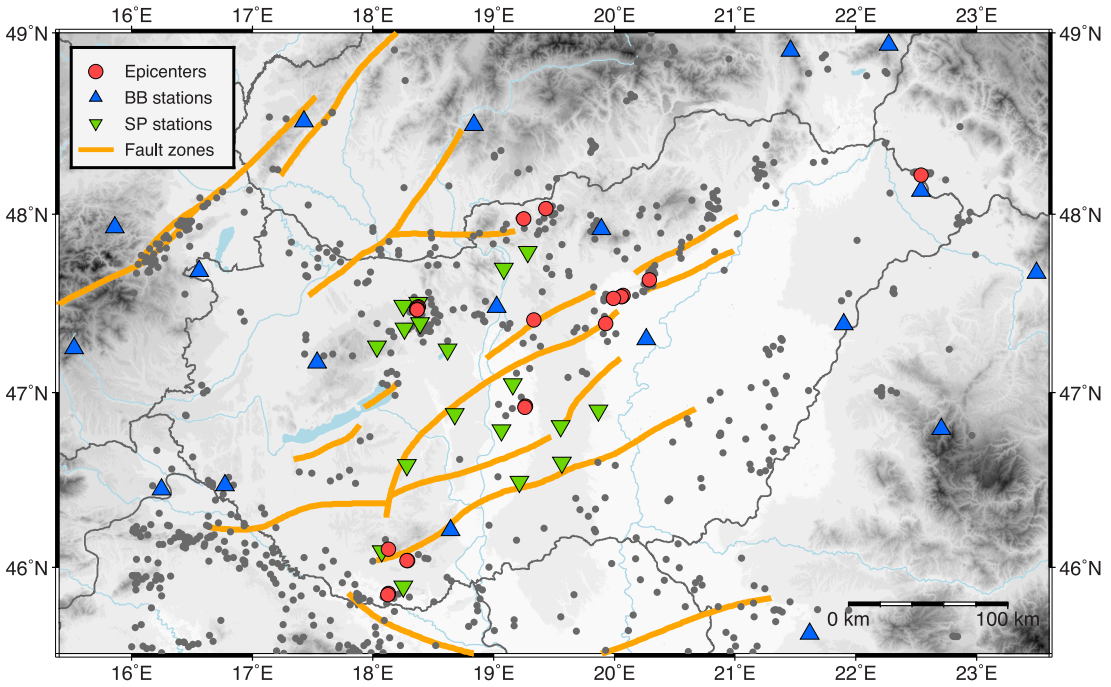

Figure 1. Map of Hungary showing the location of the seismic stations used in this study (blue triangles: broad-band stations; green inverse triangles: short-period stations) and the epicentres of the 22 earthquakes selected for waveform inversion (red circles). Grey dots indicate the background seismicity of the time period considered in this study. Thick orange lines indicate main active fault zones after Horváth *et al.* (2006).

3 DATA

3.1 Seismological observations

Waveform data used in the present study were mainly recorded by the Hungarian National Seismological Network (HNSN) and the Paks Microseismic Monitoring Network (PMMN) (Fig. 1). In the last two decades, the configuration of both networks has been changed several times: stations have been moved, added, or even removed. Consequently, the stations shown in Fig. 1 have never been in operation simultaneously. The HNSN comprised permanent broad-band stations equipped with Streckeisen STS-2 and Guralp CMG-3T seismometers with natural period of 120 s, whereas at the PMMN stations three-component 1 Hz Lennartz LE-3D geophones were deployed. For some events, seismological data from the neighbouring countries and international agencies were also available.

3.2 Event selection and data preparation

To reliably recover earthquake focal mechanisms by waveform inversion, it is necessary to use seismograms with high enough SNR observed by a station network with good azimuthal coverage. Focal mechanisms can be resolved even for small-magnitude events if these conditions are met. Specifically, the waveform inversion can be successful for weak earthquakes if the source–receiver distances are small and, as a result, the SNR of the observed waveforms is not less than 2 in the inversion frequency band.

Unfortunately, in the last two decades, the geometry of the station network in Hungary was mostly far from optimal. To find small-magnitude earthquakes with at least three recording stations at short epicentral distances and with good azimuthal coverage was generally a difficult issue. After carefully investigating the earthquake catalogue of around 1100 Hungarian events and inspecting the observed seismograms, we have finally selected 22 earthquakes with local magnitudes between 1.2 and 4.8 that occurred in the period of 1995–2014. In the future, additional events are expected to be found suitable for source inversion in this two-decade time period.

As the first step of data preparation, all the velocity seismograms were deconvolved from their instrument response and then integrated to displacement records to simplify the analysed waveforms. The records were further processed by frequency filtering. To reduce propagation effects as much as possible and get stable and robust results from the waveform inversion, it is crucial to keep the longest possible periods with a good SNR. The parameters of the filtering depended on the size of the analysed earthquake. For events with $M_L > 4$, a bandpass filter with corner frequencies of 0.05 and 0.125 Hz (periods between 8 and 20 s) was applied. Because of the poor SNR at low frequencies, smaller events had to be analysed at much higher frequencies: for earthquakes with $M_L < 4$, a bandpass filter from 0.5 to 2 Hz was used.

3.3 Event location

For locating the selected events, we manually picked *P*-wave arrival times from vertical-component seismograms and *S*-wave arrival times from horizontal-component waveforms where possible. Data from seismic stations with epicentral distance greater than about 300 km were not taken into account in the localisation procedure.

The hypocentral locations were computed using the probabilistic Non-Linear Location (NonLinLoc) software package (Lomax *et al.* 2000). We employed the oct-tree importance sampling algorithm to map the posterior probability density function (PPDF) of the earthquake location (Lomax & Curtis 2001). For calculating theoretical traveltimes, we used a recently developed one-dimensional (1-D) velocity model (Table 1) constructed from arrival-time data of earthquakes and controlled explosions for the territory of Hungary (Gráczer & Wéber 2012).

Table 1. The 1-D earth model used in this study.

h (km)	v_P (km s^{-1})	v_S (km s^{-1})	ρ (g cm^{-3})
0	5.30	3.05	2.76
3	5.74	3.30	2.85
19	6.29	3.61	2.96
26	7.93	4.56	3.29

Layer depths (h), P-wave velocities (v_P) and S-wave velocities (v_S) are after Gráczer & Wéber (2012). For density ρ, an empirical law is used: $\rho = 1.7 + 0.2v_P$, where ρ is measured in g cm^{-3} and v_P in km s^{-1}.

The retrieved hypocentral parameters of the selected 22 earthquakes are summarised in Table 2, whereas the epicentres are shown in Fig. 1. The hypocentres are generally well constrained: the calculated standard error is mostly below 1.6 km in all three dimensions. The actual discrepancy between the true and estimated hypocentres, however, is often much larger than the computed formal error. Source mislocation leads to wrong values for station azimuth and distance, which biases the resulting focal mechanisms. Therefore, in the waveform inversion we consider the hypocentral coordinates as unknown parameters. Even if we refine the hypocentres through waveform inversion, a real 3-D velocity structure can still strongly bias the resulting source mechanisms due to biased hypocentres and apparent backazimuths.

4 WAVEFORM INVERSION METHOD

In this study we used an improved version of the probabilistic nonlinear waveform inversion method of Wéber (2006, 2009) to retrieve the full moment tensor of local earthquakes. It has already been successfully applied for estimating the full moment tensor of the 2011 January 29 M_L 4.5 Oroszlány (Hungary) earthquake and its four aftershocks (Wéber & Süle 2014). The procedure works in the point-source approximation and is summarised in the following paragraphs.

A general seismic point source is described by six independent moment tensor rate functions (MTRFs). MTRF description of an earthquake allows the moment tensor to vary arbitrarily as a function of time. If the velocity structure and the hypocentral coordinates are known, there is a linear connection between the seismograms and the MTRFs. Basically, the MTRFs are obtained by deconvolving the station specific Green's functions (GFs) from the observed seismograms.

Since, in the present work, we use horizontally layered earth model to describe the real medium (Table 1), the station specific GFs can be constructed as a linear combination of elementary GFs that are independent of the event-station azimuth. Thus, the elementary GFs can be pre-computed for a discrete set of source depths and epicentral distances, and stored in a database on disk. Finally, the station specific GFs needed for the waveform inversion are determined by a linear combination of the elementary GFs taking into account the event-station azimuth as well. This approach makes the inversion very efficient because forward modelling, the most time-consuming step of the inversion, requires only very simple calculations. For constructing the elementary GFs, we used the software tools included in the 'Computer Programs in Seismology' package (Herrmann 2013). We applied the propagator matrix–wavenumber integration method, which allows for the calculation of the full waveform at high frequencies and short epicentral distances.

The waveform inversion procedure applied in this study consists of the following main steps (Fig. 2).

Step 1: The hypocentre of the event is estimated from observed arrival times by a method that provides both the hypocentral coordinates and their uncertainties. Here we used the probabilistic NonLinLoc software package (Lomax *et al.* 2000).

Step 2: Especially in case of short epicentral distances, source mislocation can significantly bias the results of any moment

Table 2. Estimated hypocentral parameters of the studied earthquakes.

Event number	Date (yyyy-mm-dd)	Time (hh:mm:ss)	Lon. (°E)	Lat. (°N)	Depth (km)	σ_{lon} (km)	σ_{lat} (km)	σ_{depth} (km)	M_L
1	1995-06-09	15:57:02	19.262	46.922	10.7	0.775	0.987	3.544	1.6
2	1996-03-28	06:31:22	19.259	46.914	12.2	0.792	0.902	1.354	3.0
3	2001-05-25	15:15:49	18.127	45.848	12.6	1.259	1.504	1.804	1.7
4	2001-06-08	09:58:56	18.121	45.840	12.9	1.305	1.549	1.798	1.2
5	2002-10-12	18:49:11	20.062	47.541	12.9	1.359	0.604	1.115	3.3
6	2002-10-23	02:52:15	20.073	47.545	13.1	1.604	0.729	1.187	3.7
7	2003-06-21	20:05:58	20.058	47.541	12.1	1.091	0.666	0.930	3.7
8	2003-06-27	01:19:20	19.992	47.531	11.5	0.902	0.509	0.887	2.4
9	2003-08-31	22:57:21	18.127	46.105	4.1	0.925	1.253	1.235	1.9
10	2003-12-31	20:43:49	18.288	46.037	3.9	0.694	0.786	1.379	2.6
11	2003-12-31	21:36:02	18.283	46.037	5.9	1.208	1.613	1.970	1.6
12	2004-06-19	10:48:07	19.930	47.390	10.5	1.233	0.460	1.121	2.5
13	2006-11-23	07:15:21	22.541	48.218	10.6	1.608	0.683	0.721	4.5
14	2006-12-31	13:39:24	19.331	47.410	3.0	1.350	1.240	1.850	4.1
15	2011-01-29	17:41:38	18.375	47.482	5.1	0.483	0.831	0.963	4.5
16	2011-01-30	13:34:29	18.367	47.480	2.8	0.699	1.430	1.478	2.0
17	2011-01-30	20:58:46	18.363	47.471	5.4	0.528	1.139	1.476	2.7
18	2011-01-31	00:25:29	18.365	47.469	5.2	0.525	1.149	1.431	2.4
19	2011-03-11	01:45:24	18.365	47.467	6.6	0.474	0.485	0.699	2.3
20	2013-04-22	22:28:47	20.289	47.634	5.1	0.576	0.756	1.265	4.8
21	2013-06-05	18:45:47	19.246	47.975	3.0	0.586	0.744	1.178	4.1
22	2014-01-19	01:34:34	19.430	48.032	3.0	0.418	0.497	1.023	4.2

σ_{lon}, σ_{lat}, σ_{depth}: standard deviation of longitude, latitude and depth, respectively; M_L: local magnitude. Hypocentres for events 15–19 are after Wéber & Süle (2014).

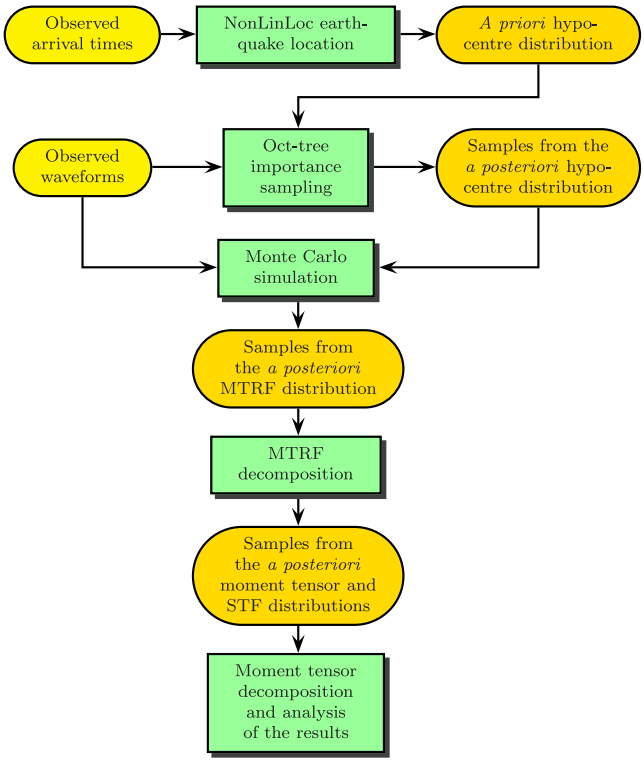

Figure 2. Flow diagram of the probabilistic waveform inversion procedure used in this study.

tensor inversion procedure. Therefore, we should further refine the hypocentral coordinates using waveform data. Thus we consider the hypocentre distribution estimated in Step 1 as *a priori* information and perform a Bayesian inverse calculation to improve the hypocentral location. Following Tarantola (1987), the PPDF of the hypocentral coordinates, $\sigma(\mathbf{h})$, is the product of two terms. The *a priori* PDF $\rho(\mathbf{h})$ incorporates information about the hypocentral position that is obtained from arrival times in Step 1. The second term, the likelihood function $L(\mathbf{h})$, measures the fit between the observed and predicted waveforms. If we adopt the Gaussian model, the *a priori* distribution is given by

$$\rho(\mathbf{h}) \propto \exp\left[-\frac{1}{2}(\mathbf{h}-\mathbf{h}_{\mathbf{prior}})^T \mathbf{C}_{\mathbf{H}}^{-1}(\mathbf{h}-\mathbf{h}_{\mathbf{prior}})\right] \quad (1)$$

whereas the likelihood function is given by

$$L(\mathbf{h}) \propto \exp\left[-\frac{1}{2}(\mathbf{g}(\mathbf{h})-\mathbf{d}_{\mathbf{obs}})^T \mathbf{C}_{\mathbf{D}}^{-1}(\mathbf{g}(\mathbf{h})-\mathbf{d}_{\mathbf{obs}})\right] \quad (2)$$

where $\mathbf{h}$ is the vector containing the hypocentral coordinates, $\mathbf{h}_{\mathbf{prior}}$ the centre of the *a priori* PDF, $\mathbf{C}_{\mathbf{H}}$ the *a priori* model covariance matrix, $\mathbf{d}_{\mathbf{obs}}$ the observed waveforms, $\mathbf{C}_{\mathbf{D}}$ the data covariance matrix (representing modelling and observational errors) and $\mathbf{g}(\mathbf{h})$ the forward modelling operator that generates the displacement field for a given hypocentre.

Proper assessment of the data covariance matrix $\mathbf{C}_{\mathbf{D}}$ in eq. (2) is not an easy task. In this study we used a simple diagonal matrix and adopted the conclusion of Zahradnik & Custódio (2012) that realistic data errors have the same order of magnitude of the data itself, mostly due to inaccurate crustal models.

For mapping the PPDF $\sigma(\mathbf{h})$, we apply the oct-tree importance sampling algorithm developed by Lomax & Curtis (2001). As a result, we get a large number of points that are samples from the PPDF of the hypocentre. For all these samples, the MTRFs are also calculated. Their distribution represents the uncertainty of the MTRFs due to that of the source location.

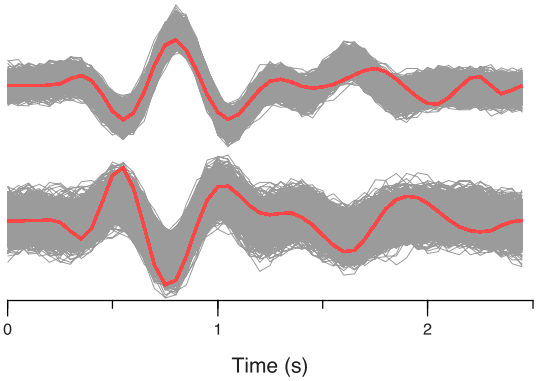

Figure 3. One thousand realizations (grey lines) of noisy waveforms (red lines) for Monte Carlo simulation. For a well-fitted seismogram (upper trace) the new realizations are close to the observation, whereas for a less-fitted waveform (lower trace) they show larger dispersion. For details see the text.

Step 3: Measurement errors and modelling errors also lead to MTRF uncertainty even for a fixed source position. To estimate the overall uncertainties of the retrieved MTRFs, we use a Monte Carlo simulation technique (Rubinstein & Kroese 2008). Monte Carlo simulation is a method for analysing uncertainty propagation, where the goal is to determine how random variation or error in the input data affects the uncertainty of the output. In our problem, source location and seismograms represent the input data, whereas MTRFs are the output. In the course of the simulation, we generate many new realizations of input data sets by randomly generating new hypocentres and waveforms according to their respective distributions. Then each generated input data set is inverted for MTRFs. The distribution of the obtained set of solutions approximates well the PPDF of the MTRFs.

After having mapped the PPDF of the source location in Step 2, generating a random hypocentre for the Monte Carlo simulation is straightforward. For generating individual realizations of noisy seismograms, we first calculate the waveform residual corresponding to the best MTRF solution obtained in Step 2. We consider this residual as a realization of the measurement and modelling errors. We convolve this error sample with a uniform white noise yielding a sample of simulated error: it is a time sequence which differs from the original sample of error but has the same amplitude spectrum. Then, we add the simulated error to the observed seismograms and obtain a new realization of waveforms which we invert for the MTRFs. For well-fitted seismograms the new realizations are close to the observations, whereas for less-fitted waveforms they show larger dispersion (Fig. 3).

In this study, we performed 10 000 Monte Carlo simulations and thus generated 10 000 MTRFs according to the *a posteriori* distribution.

Step 4: Assuming that the focal mechanism is constant in time, the previously obtained MTRFs are decomposed into a time-invariant moment tensor and a source time function (STF). The problem is non-linear and is solved by an iterative L_1 norm minimisation technique (Wéber 2009). To allow only forward slip during the rupture process, we impose a positivity constraint on the STF. After the decomposition of the MTRFs, a large number (actually 10 000 in this study) of moment tensor and STF solutions are obtained that can be considered as samples from their respective PPDFs. The final estimates are given by the maximum likelihood points.

Step 5: Once the moment tensors are retrieved, their principal axes are deduced. Then each moment tensor is decomposed into an isotropic (ISO) part, representing an explosive or implosive component, and into a deviatoric part, containing both the double-couple (DC) and the compensated linear vector dipole (CLVD) components (Jost & Herrmann 1989). Finally, the distributions of the retrieved source parameters are displayed as histogram plots.

The above described procedure can also be used when the STF is assumed to be known. In that case, Monte Carlo simulation directly results in samples from the PPDF of the moment tensor.

In this study, the method of Riedesel & Jordan (1989) is employed to display the moment tensor solution. The principal vectors of a moment tensor define the tension (T), neutral (N) and compression (P) axes, while the principal values (λ_1, λ_2, λ_3) give their magnitudes. Here we adopted the convention of Sipkin (1993) that the P and T axes always point upwards and the principal axes form a right-handed coordinate system. In the principal axis system, various unit vectors can be constructed using various linear combinations of the principal vectors. The vector that describes a general source mechanism is **m**, a DC source mechanism has the vector representation **d**, the vector corresponding to a purely ISO source is the vector **i** and two possible CLVD vectors, $\mathbf{l}_1$ and $\mathbf{l}_2$, can also be defined. The density plot (2-D histogram) of the **m** vector, together with the **d**, **i** and $\mathbf{l}_{1,2}$ vectors corresponding to the best moment tensor solution are then plotted on the surface of the focal sphere. The great circle that connects the **d** and $\mathbf{l}_{1,2}$ vectors on the unit sphere defines the subspace of deviatoric sources. The distribution of the density plot of **m** with respect to the **d**, **i** and $\mathbf{l}_{1,2}$ vectors informs us on the statistical significance of the DC, ISO and CLVD components of the solution.

The scalar seismic moments of the ISO and deviatoric components of a general moment tensor **M** are determined according to Bowers & Hudson (1999):

$$M_{\mathrm{ISO}} = \frac{1}{3} \cdot |\mathrm{Tr}(\mathbf{M})| \tag{3}$$

$$M_{\mathrm{DEV}} = \max(|\lambda_i^*|;\ i = 1, 2, 3) \tag{4}$$

where $\mathrm{Tr}(\mathbf{M}) = \lambda_1 + \lambda_2 + \lambda_3$ denotes the trace of the moment tensor **M** and $\lambda_i^* = \lambda_i - \mathrm{Tr}(\mathbf{M})/3$. Then, to assess the relative amounts of the DC, CLVD and ISO components in a moment tensor, we calculate their percentages in the following way:

$$\mathrm{ISO} = \frac{M_{\mathrm{ISO}}}{M_{\mathrm{ISO}} + M_{\mathrm{DEV}}} \times 100 \text{ (per cent)} \tag{5}$$

$$\mathrm{CLVD} = 2\frac{\left|\lambda^*_{|\mathrm{min}|}\right|}{\left|\lambda^*_{|\mathrm{max}|}\right|} \times (100 - \mathrm{ISO}) \text{ (per cent)} \tag{6}$$

$$\mathrm{DC} = 100 - \mathrm{ISO} - \mathrm{CLVD} \text{ (per cent)} \tag{7}$$

where subscripts |min| and |max| refer to the minimum and the maximum of the absolute values of λ_i^*. The ISO and CLVD components are called the non-DC components of **M**. Due to errors and incompatibilities in the observed seismograms, as well as the inaccurate knowledge of the GFs, waveform inversion always produces earthquake mechanisms with non-DC components.

We also compute the moment magnitude M_w from the scalar seismic moment M_0 according to the definition of Hanks & Kanamori (1979):

$$M_w = \frac{2}{3}\log M_0 - 6.03 \tag{8}$$

where M_0 is measured in Nm. In contrast to local magnitudes, the moment magnitude scale does not saturate for large events. The calibration of other magnitude scales on M_w is crucial for comparing earthquake data from different sources. In addition, since modern probabilistic seismic hazard analysis methods rely on magnitudes calibrated on M_w, a catalogue of reliable moment magnitudes covering a broad range in earthquake size is crucial to get correct hazard estimates.

5 WAVEFORM INVERSION RESULTS

5.1 Long-period inversion

For the analysed earthquakes with $M_L > 4$ (events 13–15 and 20–22 in Table 2), signal energy at long periods was sufficient to use long-period seismograms in the waveform inversion. Both the observed displacement waveforms and the GFs were bandpass filtered with a Butterworth filter with a low corner of 0.05 Hz and a higher corner at 0.125 Hz (corner periods of 20 and 8 s, respectively). We used data observed by broad-band stations. The seismograms suitable for inversion were manually selected based on the SNR in the above frequency band. The processed time window started at 5 s before the arrival of the first P phase and its length was varied between 50 and 110 s depending on the epicentral distance. The synthetic waveforms (GFs) were windowed in the same way as the observed ones. Because differences between the true earth structure and our 1-D model considerably affect the arrival time of seismic phases, before performing the waveform inversion we applied a time-shift between the synthetics and the data to obtain the optimal correlation between them.

Since the inversion frequency band is well below the corner frequency of the investigated events, we assumed that the STF was a known parameter and it had a 4-second triangular shape. When the STF is considered as a known parameter, the Monte Carlo simulation described in the previous section directly results in samples from the posterior moment tensor distribution.

The waveform inversion results for the investigated $M_L > 4$ events are listed in Table 3 and plotted in Fig. 4. The figure shows the beach ball representation of the deviatoric part of the full moment tensor solutions together with the density plots (2-D histograms) of the P and T principal axes. In addition, the density plots of the resulting full moment tensors are also illustrated in Fig. 5. The scalar seismic moments and principal axes of the maximum likelihood mechanisms are presented in Table 5 together with their 95 per cent confidence intervals.

According to Fig. 4 and Table 5, for events 13–15 and 21–22, both the P and T axes are strongly clustered around well-defined directions. For event 20, the density plot of the P axis is well confined, whereas the T axis is less well constrained. The Riedesel–Jordan (RJ) plots of the moment tensor distribution (Fig. 5) also illustrate that the moment tensor solution for event 20 has the largest uncertainty among the six $M_L > 4$ events. Nevertheless, the plots suggest that the moment tensor solutions are robust and of sufficient quality to allow a tectonic interpretation.

Table 3 shows that the DC component varies between 84 and 97 per cent, and the CLVD and ISO components are below 10 per cent. Indeed, the DC vector lies within the density plot of the moment tensor for all the $M_L > 4$ earthquakes (Fig. 5) suggesting that the non-DC components have no statistical significance and pure DC mechanisms can be considered as the solutions for these events.

Table 3. Maximum likelihood centroids, source mechanisms and moment magnitudes (M_w) determined by long-period waveform inversion.

Event number	M_w	Lon. (°E)	Lat. (°N)	Depth (km)	Strike (°)	Dip (°)	Rake (°)	DC (per cent)	CLVD (per cent)	ISO (per cent)	μ	Agency
13	4.3	22.553	48.219	7	301/36	80/64	−26/−169	91	3	6	–	
	4.4	22.550	48.320	12	133/37	80/61	30/169	50	50	–	0.20	INGV
14	3.9	19.343	47.420	5	276/185	81/81	9/171	97	1	2	–	
15	4.4	18.374	47.476	5	179/88	84/83	−173/−6	90	2	8	–	
	4.2	18.320	47.560	15	355/265	90/80	−170/0	100	–	–	0.17	NEIC
	4.3	18.269	47.450	13	2/93	84/79	169/6	57	43	–	0.13	GFZ
	4.4	18.340	47.490	17	187/96	81/83	−172/−9	63	37	–	0.14	INGV
20	4.7	20.291	47.642	3	319/169	44/50	68/110	86	5	9	–	
	4.4	20.238	47.633	5	304/142	62/29	81/107	82	18	–	0.33	NEIC
21	4.0	19.248	47.972	3	76/345	77/86	4/167	93	2	5	–	
	3.9	19.240	47.970	10	263/360	74/67	−23/−162	96	4	–	0.36	GFZ
22	4.2	19.429	48.031	5	175/84	86/70	−160/−4	84	8	8	–	
	4.0	19.348	48.053	4	344/75	69/87	177/21	65	35	–	0.29	NEIC

Solutions published by other agencies are also indicated. To measure the difference between our solutions and those published by other agencies, the parameter μ defined by Pasyanos *et al.* (1996) is used. For values of $\mu < 0.25$, the focal mechanisms are essentially the same, but start to diverge for $0.25 < \mu < 0.50$. Event numbers refer to those in Table 2.

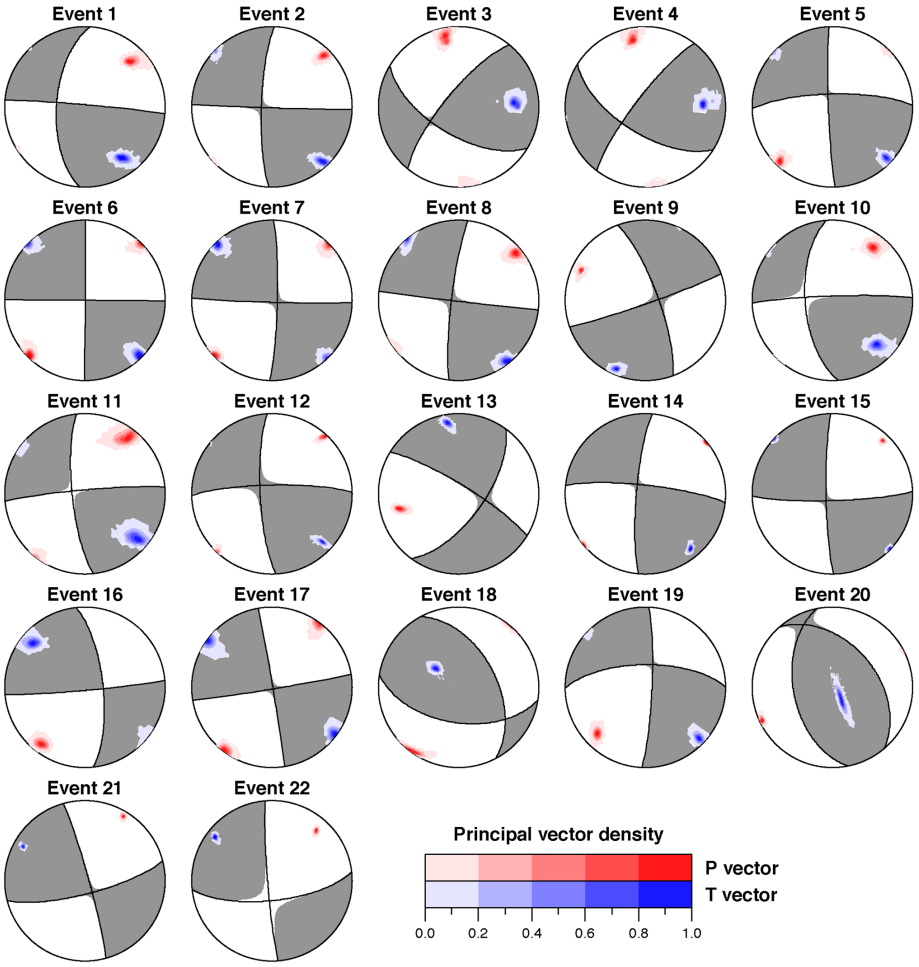

Figure 4. Source mechanisms of the 22 investigated earthquakes obtained by waveform inversion. The beach balls represent the deviatoric part of the mechanisms (shaded area: compression; open area: dilatation). The density plots of the *P* (red) and *T* (blue) principal axes are plotted on top of the beach balls. Equal area projection of lower hemisphere is used. Event numbers refer to those in Table 2.

To illustrate the achieved quality of waveform fitting, Fig. 6 compares the observed seismograms of event 22 ($M_L = 4.2$) and the synthetic waveforms computed using the best (maximum likelihood) source parameters. Two quantities are given for each seismogram: the normalized correlation coefficient c and the variance reduction $vr = 1 - \sum_i r_i^2 / \sum_i d_i^2$, where r_i and d_i are samples of the residual vector and the data vector, respectively. Because of the good SNR in the inversion frequency band and the azimuthally well-distributed

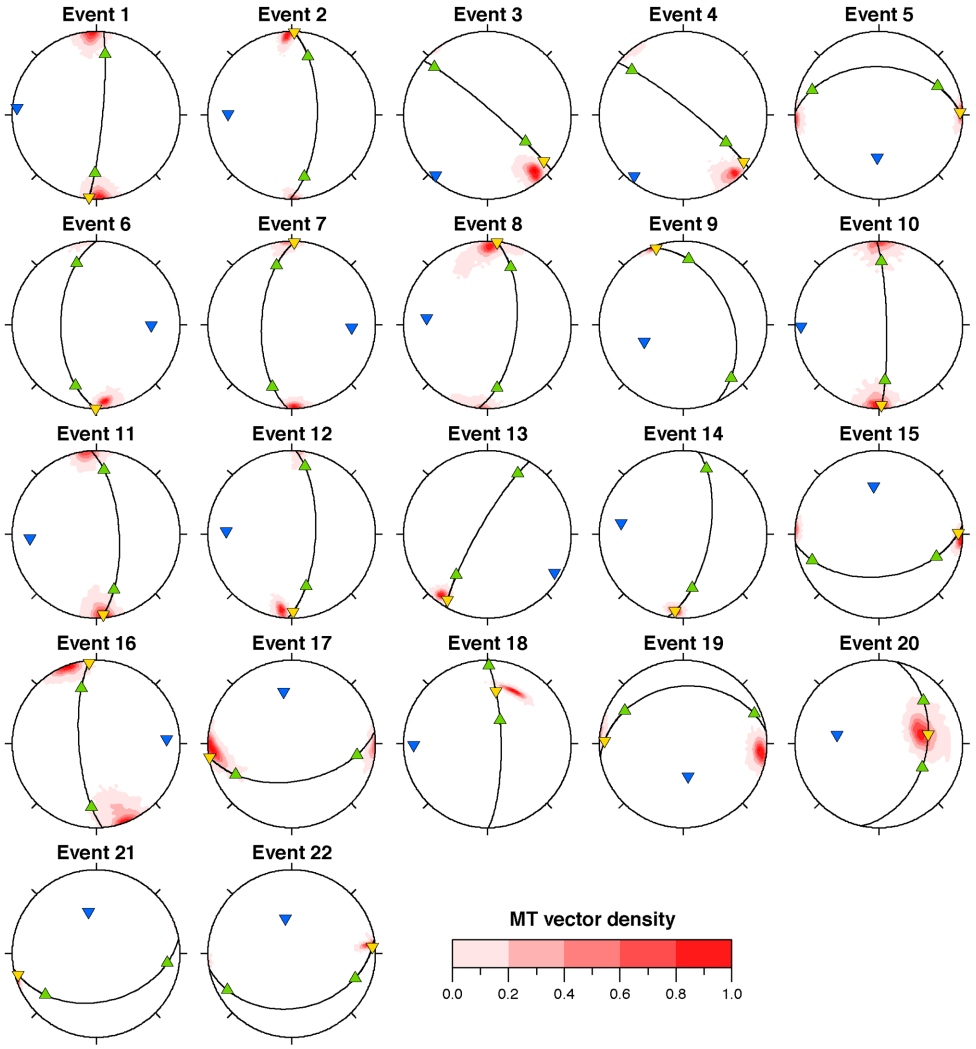

Figure 5. Density plots of the moment tensors obtained for the 22 analysed earthquakes. For display purposes, the method of Riedesel & Jordan (1989) is employed (orange inverse triangle: **d** vector for the DC component; green triangles: $\mathbf{l}_{1,2}$ vectors for the CLVD components; blue inverse triangle: **i** vector for the isotropic part). The great circle connecting the **d** and $\mathbf{l}_{1,2}$ vectors defines pure deviatoric mechanisms. Equal area projection of lower hemisphere is used. Event numbers refer to those in Table 2.

recording stations, the waveforms are fitted fairly well. Waveform fitting for all the analysed earthquakes are shown in the supporting information available online.

In the online catalogues of the U.S. Geological Survey (USGS) National Earthquake Information Center (NEIC), the German Research Centre for Geosciences (GFZ) and the Istituto Nazionale di Geofisica e Vulcanologia (INGV), regional moment tensor solutions have been published for five of the $M_L > 4$ events investigated here. These regional moment tensors show very good agreement with the source mechanisms retrieved in this study (Fig. 7 and Table 3).

To quantitatively compare our solutions to those published by the above agencies, we follow Pasyanos *et al.* (1996) using their moment tensor difference parameter μ defined as the root mean square of the differences of the moment tensor elements normalized by their respective scalar moment M_0:

$$\mu = \sqrt{\frac{1}{8}\sum_{i=1}^{3}\sum_{j=1}^{3}(\delta M_{ij}^{'})^2} \tag{9}$$

where $\delta M_{ij}^{'} = M_{ij}^{(1)}/M_0^{(1)} - M_{ij}^{(2)}/M_0^{(2)}$. Focal mechanisms with $\mu < 0.25$ are essentially the same but start to diverge for $0.25 < \mu < 0.50$, whereas $\mu > 0.50$ indicates significantly different mechanisms.

As seen from Table 3, for events 13 and 15 the μ values are well below 0.25 confirming that the agency solutions are practically identical to ours. For event 22, the USGS NEIC mechanism differs only slightly ($\mu = 0.29$) from the solution of this study. For event 20, the difference is more pronounced ($\mu = 0.33$). Indeed, the strike of the USGS NEIC mechanism notably varies from that of our solution. However, both mechanisms agree equally well with the available clear readings of first-arrival *P*-wave polarities (Fig. 7). We calculated the largest μ-value (0.36) for event 21, where both the strike and the dip of the GFZ solution differ from those achieved in this research. We consider our solution to be better, as it better agrees with the available first-arrival *P*-wave polarities (Fig. 7).

5.2 Short-period inversion

Low-magnitude ($M_L < 4$) earthquakes are usually too small to provide enough information (above noise level) at long periods but are well recorded at relatively high frequencies. However, short wavelengths are more affected by small-scale heterogeneities of the

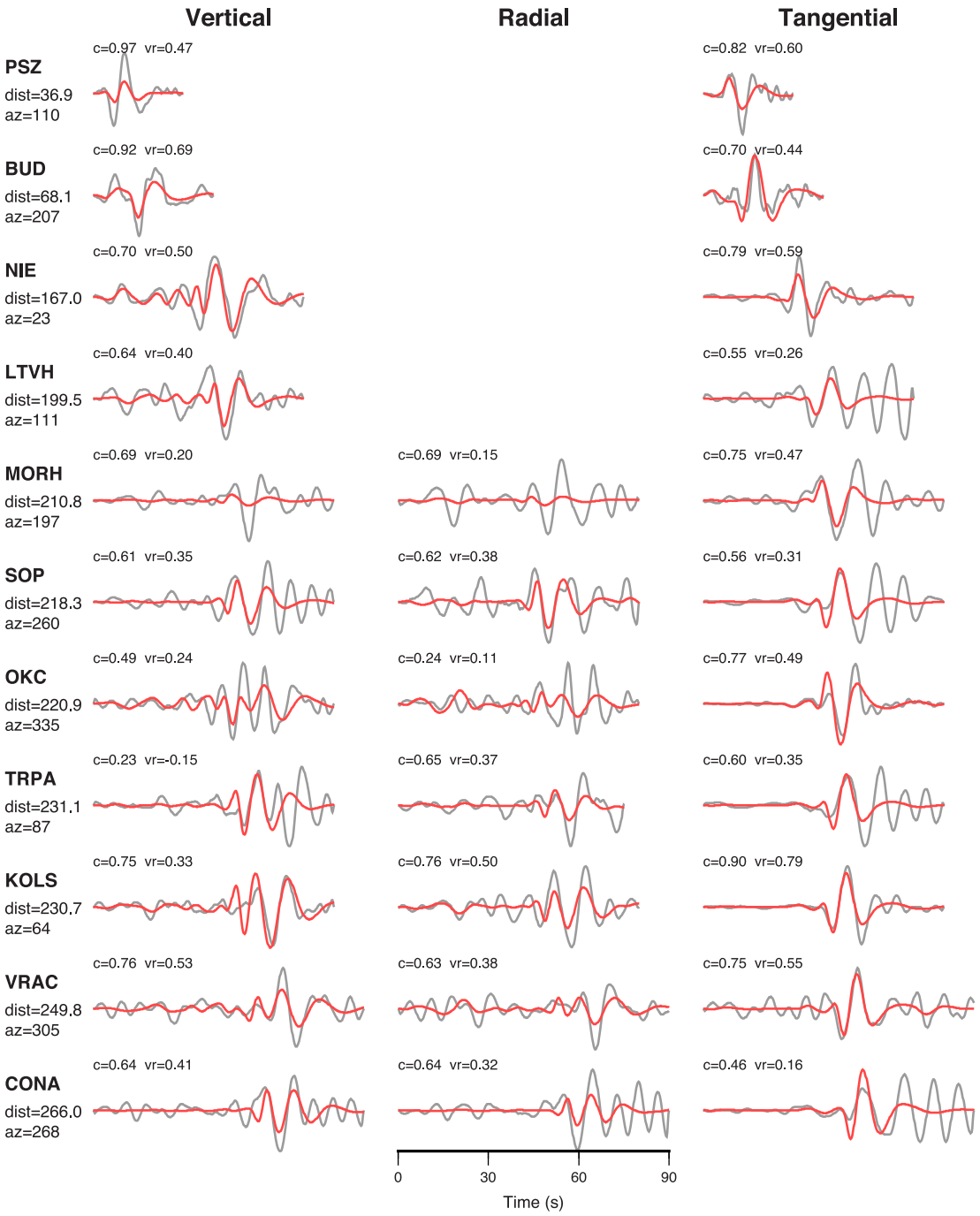

Figure 6. Waveform comparison for event 22 ($M_L = 4.2$). The observed seismograms (grey lines) are bandpass filtered with cut-off frequencies of 0.05 and 0.125 Hz. The synthetic waveforms (red lines) are computed using the maximum likelihood source parameters obtained by waveform inversion. On the left-hand side of each row, station code, epicentral distance in km (dist) and station azimuth (az) are indicated. The numbers above each waveform represent the normalized correlation (c) and variance reduction (vr).

medium not modelled in our simple 1-D velocity model, so the high-frequency content of the waveforms to be inverted should be kept at a minimum. On the other hand, the value of the lower cut-off frequency is mainly determined by the SNR at long periods and by the natural frequencies of the short-period stations. Eventually, for the $M_L < 4$ earthquakes, we applied a causal bandpass filter from 0.5 to 2 Hz to the observed displacement waveforms before inversion. The same filter was applied to the displacement GFs. Recently, Wéber & Süle (2014) have shown that the waveform inversion method employed in this study is suitable to estimate reliable earthquake moment tensors using waveform data in this frequency range.

At high frequencies, our simple 1-D earth model allows us to model sufficiently the beginning of the *P*- and *S*-wave trains, but it is not detailed enough to properly predict later phases created by a real 3-D velocity structure. For this reason, in the inversion procedure we used first-arrival body waves only. For the vertical and radial components, the processed time window started at the arrival of the *P*-phase, whereas for the transverse component it started at the *S*-phase. The length of the time window was chosen according

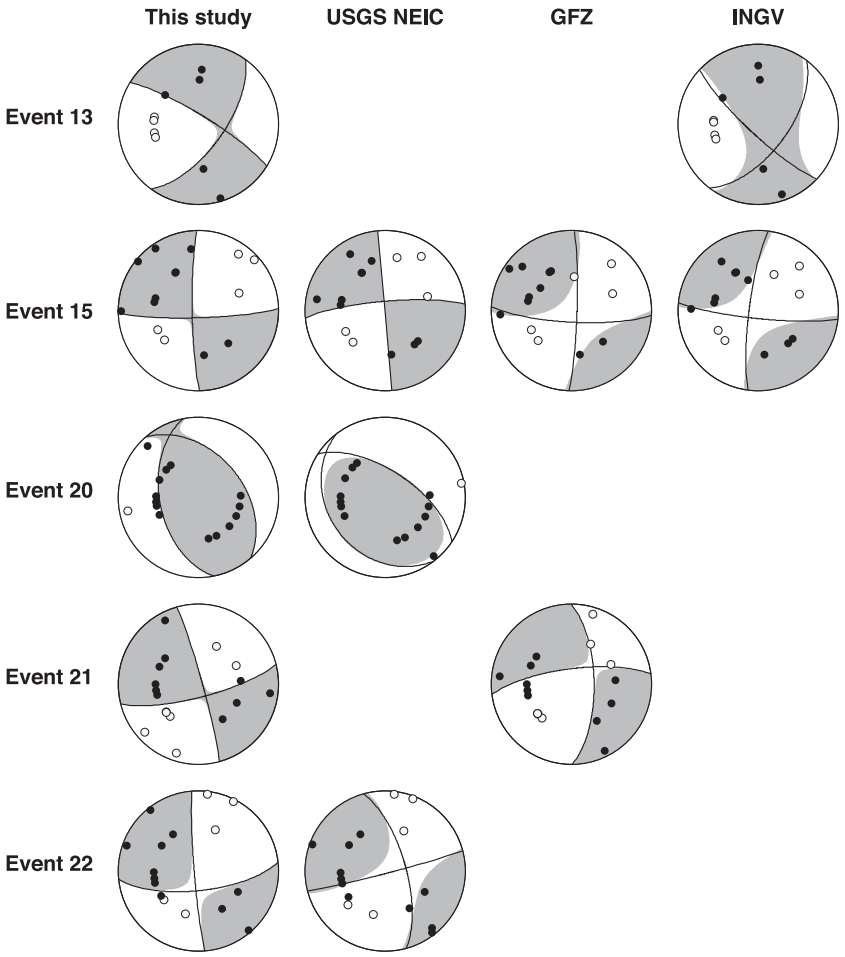

Figure 7. Comparison of the moment tensor solutions obtained in this study with those reported by the USGS NEIC, the GFZ and the INGV for five of the analysed $M_L > 4$ earthquakes. Only deviatoric components are shown (shaded area: compression; open area: dilatation). First-arrival *P*-wave polarities are indicated as well (solid circle: compression; open circle: dilatation). Equal area projection of lower hemisphere is used. Event numbers refer to those in Table 2.

to the epicentral distance but it was shortened for some stations when it became evident that the latter part of the seismograms had not been recovered satisfactorily. The used 1-D velocity model is also not accurate enough to predict the observed arrival times, so to obtain the optimal correlation between the synthetics and the data, before inversion we applied a time-shift between them. We allowed different time-shifts for the *P*-phase and the *S*-phase.

When inverting short-period waveforms, we considered the STF as an unknown parameter. The STFs obtained by inversion are very simple: they all have a single peak significant at the 95 per cent confidence level. Fig. 8 shows four STF solutions typical in this study.

The source mechanisms calculated for the analysed $M_L < 4$ earthquakes are listed in Tables 4 and 5 and plotted in Fig. 4, whereas the RJ plots are depicted in Fig. 5.

As seen from Figs 4 and 5, the uncertainties of the solutions for the $M_L < 4$ events are notably greater than those obtained for the $M_L > 4$ earthquakes. It may be due to the fact that small-magnitude events are usually recorded by only a few seismic stations with SNR ≥ 2 in the inversion frequency band. Additionally, the simple 1-D earth model applied in the inversion procedure can introduce considerable modelling errors at high frequencies, increasing the uncertainties of the resulting moment tensors. Nevertheless, both the *P* and *T* principal axes are well constrained and clustered around well-defined directions for all the mechanisms (Table 5).

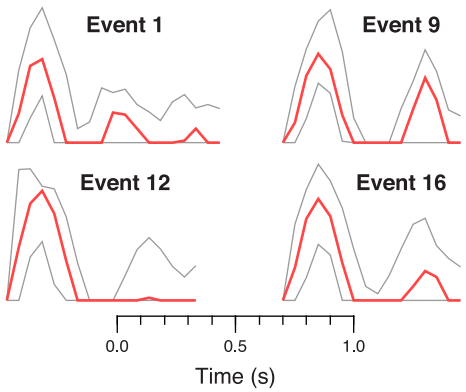

Figure 8. Four typical source time functions (STFs) obtained by short-period waveform inversion. The thin grey lines illustrate the 95 per cent confidence region. The STFs have a single peak significant at this confidence level. Event numbers refer to those in Table 2.

Table 4 shows that the DC component varies between 81 and 98 per cent and the CLVD component does not exceed 5 per cent. The ISO content is mostly not more than 10 per cent but for a couple of events it exceeds 15 per cent. However, the DC vector lies within the density plot of the moment tensor for all the investigated $M_L < 4$ earthquakes (Fig. 5) implying that the non-DC components

Table 4. Maximum likelihood centroids, source mechanisms and moment magnitudes (M_w) determined by short-period waveform inversion.

Event number	M_w	Lon. (°E)	Lat. (°N)	Depth (km)	Strike (°)	Dip (°)	Rake (°)	DC (per cent)	CLVD (per cent)	ISO (per cent)
1	2.0	19.257	46.909	14	275/184	88/61	29/177	90	0	10
2	2.7	19.254	46.912	13	92/182	89/80	−10/−179	91	2	7
3	2.1	18.128	45.856	11	219/121	76/62	29/164	89	1	10
4	2.1	18.122	45.846	12	217/122	80/63	28/169	90	0	10
5	2.8	20.065	47.539	14	178/269	86/77	167/4	98	1	1
6	3.2	20.085	47.544	14	270/0	90/89	−1/−180	92	0	8
7	3.1	20.073	47.540	14	92/1	88/84	6/178	90	2	8
8	2.1	19.987	47.532	15	97/187	89/83	−7/−179	92	3	5
9	2.5	18.109	46.120	7	71/340	86/77	−167/−4	96	4	0
10	2.4	18.279	46.033	10	268/176	86/62	28/175	91	5	4
11	1.8	18.274	46.034	9	265/174	86/77	13/176	97	2	1
12	2.3	19.956	47.390	13	269/177	81/78	12/171	83	5	12
16	2.0	18.372	47.458	9	354/85	71/87	177/19	82	1	17
17	2.4	18.364	47.479	8	351/81	89/88	178/1	89	2	9
18	2.3	18.363	47.473	8	332/99	51/54	130/52	81	1	18
19	2.3	18.379	47.462	8	2/270	83/67	−157/−7	82	1	17

Solutions for events 16–19 are after Wéber & Süle (2014). Event numbers refer to those in Table 2.

Table 5. Scalar moments and principal axes of the investigated earthquakes together with their 95 per cent confidence intervals.

Event number	M_0 (Nm)	*T* axis		*N* axis		*P* axis		Faulting type
		Azimuth (°)	Plunge (°)	Azimuth (°)	Plunge (°)	Azimuth (°)	Plunge (°)	
1	$1.311^{+0.437}_{-0.251} \times 10^{12}$	323^{+8}_{-7}	-22^{+15}_{-8}	279^{+37}_{-31}	61^{+13}_{-12}	226^{+11}_{-6}	-18^{+15}_{-9}	99 per cent SS, 1 per cent U
2	$1.395^{+0.509}_{-0.329} \times 10^{13}$	317^{+4}_{-6}	-7^{+14}_{-13}	266^{+55}_{-90}	79^{+7}_{-16}	226^{+4}_{-5}	-8^{+9}_{-12}	100 per cent SS
3	$1.652^{+1.437}_{-0.507} \times 10^{12}$	263^{+10}_{-7}	-31^{+11}_{-7}	243^{+36}_{-21}	58^{+11}_{-9}	168^{+8}_{-5}	-9^{+17}_{-14}	98 per cent SS, 2 per centTS
4	$1.672^{+1.695}_{-0.578} \times 10^{12}$	263^{+9}_{-6}	-26^{+17}_{-10}	236^{+43}_{-21}	61^{+18}_{-12}	167^{+9}_{-4}	-11^{+17}_{-11}	99 per cent SS, 1 per cent U
5	$1.677^{+0.485}_{-0.291} \times 10^{13}$	313^{+5}_{-3}	-12^{+18}_{-5}	162^{+130}_{-85}	-76^{+8}_{-12}	44^{+5}_{-4}	-6^{+10}_{-11}	100 per cent SS
6	$8.026^{+1.808}_{-1.263} \times 10^{13}$	135^{+6}_{-5}	0^{+20}_{-9}	0^{+154}_{-135}	90^{+0}_{-22}	45^{+7}_{-5}	-1^{+12}_{-12}	100 per cent SS
7	$5.826^{+1.306}_{-1.091} \times 10^{13}$	137^{+5}_{-5}	-5^{+16}_{-10}	109^{+170}_{-166}	84^{+5}_{-13}	46^{+5}_{-5}	-3^{+15}_{-6}	100 per cent SS
8	$1.692^{+0.468}_{-0.231} \times 10^{12}$	322^{+7}_{-8}	-4^{+14}_{-9}	269^{+82}_{-89}	83^{+5}_{-16}	231^{+7}_{-6}	-6^{+9}_{-16}	100 per cent SS
9	$6.113^{+1.732}_{-0.923} \times 10^{12}$	25^{+2}_{-7}	-7^{+5}_{-8}	265^{+16}_{-17}	-76^{+10}_{-7}	116^{+3}_{-7}	-12^{+6}_{-7}	100 per cent SS
10	$4.600^{+2.449}_{-0.568} \times 10^{12}$	315^{+7}_{-9}	-23^{+18}_{-8}	276^{+23}_{-45}	62^{+12}_{-11}	219^{+6}_{-8}	-16^{+11}_{-9}	99 per cent SS, 1 per cent U
11	$5.536^{+5.720}_{-0.440} \times 10^{11}$	310^{+8}_{-9}	-12^{+14}_{-21}	282^{+54}_{-73}	77^{+8}_{-31}	219^{+4}_{-16}	-6^{+12}_{-23}	98 per cent SS, 2 per cent U
12	$2.783^{+1.088}_{-0.599} \times 10^{12}$	313^{+4}_{-2}	-15^{+12}_{-11}	305^{+46}_{-52}	75^{+9}_{-13}	223^{+3}_{-3}	-2^{+9}_{-12}	100 per cent SS
13	$3.705^{+0.851}_{-0.632} \times 10^{15}$	171^{+6}_{-4}	-11^{+7}_{-10}	102^{+20}_{-16}	62^{+7}_{-12}	76^{+4}_{-6}	-25^{+7}_{-11}	100 per cent SS
14	$9.085^{+2.209}_{-0.999} \times 10^{14}$	320^{+3}_{-4}	-13^{+5}_{-6}	320^{+21}_{-16}	77^{+5}_{-6}	230^{+4}_{-4}	0^{+4}_{-3}	100 per cent SS
15	$4.123^{+0.712}_{-0.432} \times 10^{15}$	134^{+2}_{-2}	0^{+5}_{-3}	41^{+34}_{-23}	-81^{+5}_{-4}	224^{+2}_{-3}	-9^{+4}_{-4}	100 per cent SS
16	$1.006^{+0.600}_{-0.249} \times 10^{12}$	131^{+8}_{-8}	-15^{+21}_{-11}	94^{+26}_{-73}	71^{+7}_{-11}	38^{+8}_{-7}	-11^{+7}_{-10}	100 per cent SS
17	$3.761^{+1.936}_{-0.834} \times 10^{12}$	126^{+6}_{-6}	-2^{+17}_{-18}	317^{+169}_{-174}	-88^{+23}_{-1}	216^{+7}_{-6}	0^{+12}_{-13}	100 per cent SS
18	$2.783^{+1.054}_{-0.767} \times 10^{12}$	128^{+12}_{-7}	-60^{+8}_{-6}	124^{+11}_{-18}	30^{+7}_{-6}	35^{+10}_{-13}	-2^{+4}_{-10}	98 per cent TF, 2 per cent TS
19	$2.959^{+0.992}_{-0.483} \times 10^{12}$	314^{+4}_{-5}	-11^{+14}_{-11}	198^{+37}_{-27}	-66^{+9}_{-14}	48^{+5}_{-8}	-21^{+13}_{-6}	100 per cent SS
20	$1.100^{+0.441}_{-0.261} \times 10^{16}$	323^{+14}_{-114}	-75^{+21}_{-11}	156^{+6}_{-5}	-15^{+19}_{-21}	65^{+5}_{-3}	-3^{+5}_{-5}	98 per cent TF, 2 per cent TS
21	$9.669^{+1.240}_{-0.967} \times 10^{14}$	119^{+2}_{-2}	-12^{+4}_{-5}	327^{+14}_{-19}	-76^{+6}_{-5}	211^{+2}_{-2}	-6^{+5}_{-5}	100 per cent SS
22	$1.957^{+0.323}_{-0.388} \times 10^{15}$	128^{+2}_{-2}	-11^{+4}_{-8}	7^{+14}_{-17}	-70^{+8}_{-4}	221^{+3}_{-2}	-17^{+5}_{-6}	100 per cent SS

Plunge is positive downwards and negative upwards. Faulting types have been determined according to the classification scheme of Zoback (1992) (SS: strike-slip faulting; TS: transpression; TF: thrust faulting; U: unknown). Percentages are rounded to the nearest integer. Event numbers refer to those in Table 2.

are statistically insignificant and the solutions may be described by pure DC mechanisms.

As an example, Fig. 9 compares the observed seismograms of event 19 ($M_L = 2.3$) and the synthetic waveforms computed using the best (maximum likelihood) source parameters. The figure illustrates that for short epicentral distances, very good waveform fit can be achieved even at relatively high frequencies. Waveform fitting for all the analysed earthquakes are shown in the supporting information available online.

Eventually, we can conclude that the applied probabilistic waveform inversion procedure produced robust and well-defined moment tensor solutions that are suitable to draw conclusions on the

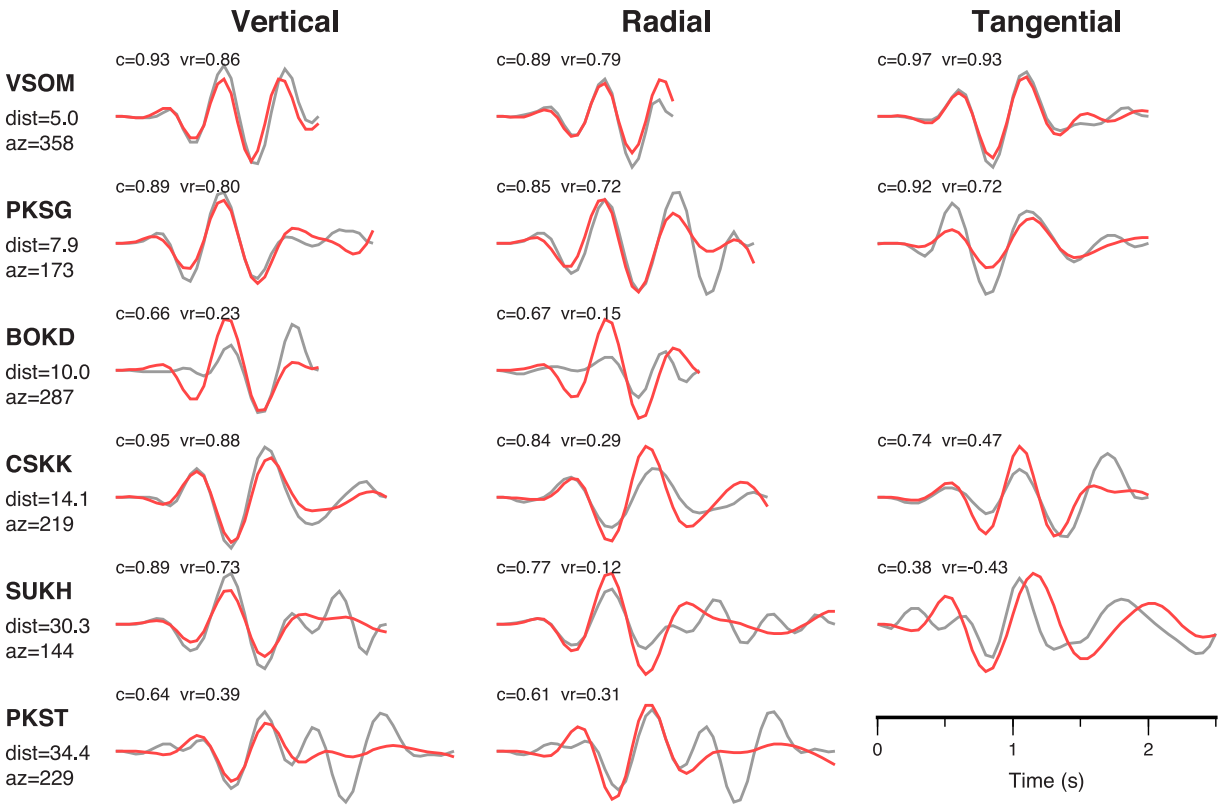

Figure 9. Waveform comparison for event 19 ($M_L = 2.3$). The observed seismograms (grey lines) are bandpass filtered with cut-off frequencies of 0.5 and 2 Hz. The synthetic waveforms (red lines) are computed using the maximum likelihood source parameters obtained by waveform inversion. On the left-hand side of each row, station code, epicentral distance in km (dist) and station azimuth (az) are indicated. The numbers above each waveform represent the normalized correlation (c) and variance reduction (vr).

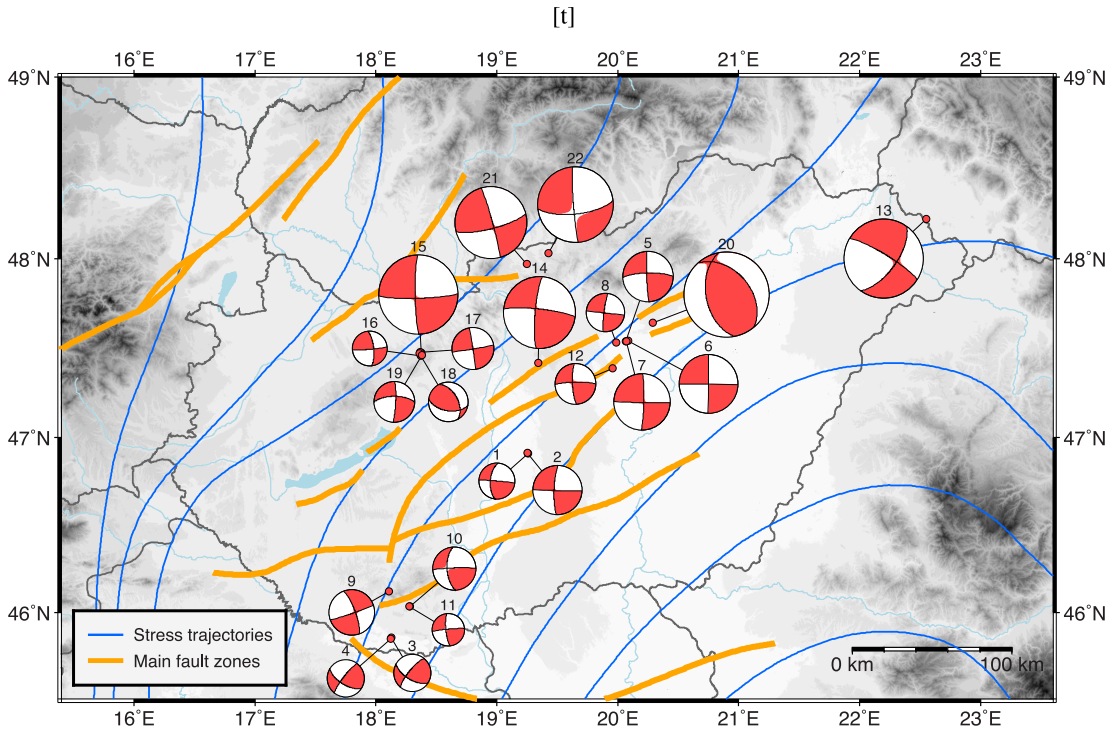

Figure 10. Source mechanisms of the analysed earthquakes on a map of Hungary. Beach ball size is proportional to event magnitude (shaded area: compression; open area: dilatation). Equal area projection of lower hemisphere is used. Event numbers above the beach balls refer to those in Table 2. Thin blue lines depict the trajectories of maximum horizontal stress directions after Bada *et al.* (2007), whereas thick orange lines indicate main active fault zones after Horváth *et al.* (2006).

neotectonic features of the epicentral regions. In Fig. 10 we summarise our source mechanism solutions on a map of Hungary.

6 DISCUSSIONS AND CONCLUSIONS

We have successfully estimated the full moment tensors of 22 earthquakes in the Hungarian part of the Pannonian basin using a probabilistic waveform inversion procedure. We have shown that the applied inversion method is equally suitable to recover the source mechanism for low-magnitude events using short-period local waveforms as well as for moderate-size earthquakes using long-period seismograms.

The non-DC components of the retrieved moment tensor solutions are statistically insignificant. The negligible amount of the ISO component implies the tectonic nature of the investigated events. In general, the obtained centroids (Tables 3 and 4) differ from the hypocentres (Table 2) just within the calculated location errors.

The compilation of moment tensor solutions displayed in Figs 4 and 10 reveals that both the P and T principal axes are predominantly horizontal and the P axis is mostly oriented along a NE-SW direction. Only 2 of the 22 analysed earthquakes (events 18 and 20) have near-vertical (plunge $> 60^\circ$) T axis with horizontal P axis.

According to Anderson (1951), the stress regime determines the dominant style of faulting through the orientation of the principal stress axes with respect to the horizontal plane. Three main stress regimes are defined: normal faulting (NF) when the P axis is vertical and T is horizontal; strike-slip (SS) when both P and T are horizontal and thrust faulting (TF) when P is horizontal and T is vertical. The World Stress Map Project also uses the intermediate cases transtension (NS) and transpression (TS) for the combination of strike-slip faulting with normal and thrust faulting, respectively. A similar classification scheme has been applied here by adopting the cut-off values for plunges of the P, T and N axes as proposed by Zoback (1992). The outcome of this classification (Table 5) reveals that most of the investigated earthquakes have strike-slip mechanism with either right-lateral slip on an approximately NS-striking, or left-lateral movement on a roughly EW-striking nodal plane. Only two events show thrust faulting mechanism, and no event is in the normal faulting regime. It is important to note that the retrieved dominant faulting types have very large probabilities ($\geq$98 per cent) for all the investigated events (Table 5). The above result suggests that compression is predominant in the central part of the Pannonian basin confirming that structural inversion is currently taking place in the region (Bada *et al.* 1999, 2001, 2007).

Bada *et al.* (2007) presented a compilation of data on the present-day stress pattern in the Pannonian basin and its tectonic environment, and constructed the trajectories of maximum horizontal stress directions depicted in Fig. 10. The derived contemporaneous stress field exhibits important lateral variations.

According to Bada *et al.* (2007), in SW Hungary the maximum horizontal stress is oriented along a NNE-SSW direction (Fig. 10). The earthquakes occurred in this region (events 3–4 and 9–11) are strike-slip events. The azimuth of the horizontal P principal axis is around 347° for events 3–4 and 39° for events 10–11. These focal mechanism orientations are concordant with the published stress direction. For event 9, however, the azimuth of the P axis is practically perpendicular to the stress trajectories. This single contradiction may be due to small-scale local tectonic effects and does not affect the overall picture of the stress field.

In NE Hungary, Bada *et al.* (2007) suggest an approximately E-W striking maximum horizontal stress direction. In this area only one $M_L = 4.5$ earthquake (event 13) has been investigated. The orientation of the P axis of this strike-slip event (azimuth = 256°) also agrees well with the main stress pattern.

In the other source regions studied in this paper, the P axes of the retrieved moment tensors are roughly oriented along a NE-SW direction ($31^\circ <$ azimuth $< 64^\circ$). Again, this result coincides well with the stress trajectories proposed by Bada *et al.* (2007).

Summing up, the orientations of the obtained focal mechanisms are in good agreement with the present-day stress field derived by Bada *et al.* (2007). The subhorizontal P axis strikes about NNE-SSW in SW Hungary, NE-SW well inside the Pannonian basin and around E-W in the NE part of the country.

Comparing the geometry of the active faults in Hungary with the predominant directions of the nodal lines of the focal mechanisms (Fig. 10), we can conclude that most of the analysed earthquakes occurred on faults or subfaults differently oriented than the main fault system. We have found only strike-slip and thrust faulting events, giving further support to the hypothesis that the Pannonian basin is currently experiencing a compressional regime of deformation. Our results thus bring important and new constraints on the geodynamic processes that are currently shaping the Pannonian region. Nevertheless, we are aware that the number of the analysed earthquakes is rather limited and the events are unevenly distributed in the area. So it will be interesting to see whether further source mechanism solutions for other parts of the country will confirm our conclusions.

ACKNOWLEDGEMENTS

The author would like to thank the different organizations that operate seismological networks in the neighbouring countries of Hungary for making their high-quality data available. I am also grateful to Georisk Ltd. for providing the waveform data recorded by the Paks Microseismic Monitoring Network. I thank S. Stähler and an anonymous reviewer for making various suggestions, which have helped me in improving this paper. Figures were prepared using the Generic Mapping Tools software (Wessel & Smith 1998).

REFERENCES

Anderson, E.M., 1951. *The Dynamics of Faulting,* Oliver and Boyd Ltd.

Babuska, V., Plomerová, J. & Sileny, J., 1987. Structural model of the subcrustal lithosphere in central Europe, in *Composition, Structure and Evolution of the Lithosphere-Asthenosphere System,* pp. 239–251, eds Fuchs, K. & Froidevaux, C., AGU Geodyn. Ser. 16.

Bada, G., Horváth, F., Cloetingh, S., Coblentz, D.D. & Tóth, T., 2001. The role of topography induced gravitational stresses in basin inversion: the case study of the Pannonian basin, *Tectonics,* **20,** 343–363.

Bada, G., Horváth, F., Dövényi, P., Szafián, P., Windhoffer, G. & Cloetingh, S., 2007. Present-day stress field and tectonic inversion in the Pannonian basin, *Glob. Planet. Change,* **58,** 165–180.

Bada, G., Horváth, F., Gerner, P. & Fejes, I., 1999. Review of the present-day geodynamics of the Pannonian basin: progress and problems, *J. Geodyn.,* **27,** 501–527.

Bowers, D. & Hudson, J.A., 1999. Defining the scalar moment of a seismic source with a general moment tensor, *Bull. seism. Soc. Am.,* **89,** 1390–1394.

Debski, W., 2008. Estimating the earthquake source time function by Markov Chain Monte Carlo sampling, *Pure appl. Geophys.,* **165,** 1263–1287.

Decker, K., Lillie, R. & Tomek, C. (eds), 1998. PANCARDI: The Lithospheric Structure and Evolution of the Pannonian/Carpathian/Dinaride Region, *Tectonophysics,* **297** (special issue), 1–293.

Dreger, D.S. & Helmberger, D.V., 1993. Determination of source parameters at regional distances with single station or sparse network data, *J. geophys. Res.,* **98,** 8107–8125.

Fodor, L. *et al.*, 2005. An outline of neotectonic structures and morphotectonics of the western and central Pannonian basin, *Tectonophysics,* **410,** 15–41.

Gerner, P., Bada, G., Dövényi, P., Müller, B., Oncescu, M.C., Cloetingh, S. & Horváth, F., 1999. Recent tectonic stress and crustal deformation in and around the Pannonian Basin: data and models, in *The Mediterranean Basins: Tertiary Extension within the Alpine Orogen,* pp. 269–294, eds Durand, B., Jolivet, L., Horváth, F. & Seranne, M., Geological Society, London, Special Publications, **156**.

Gráczer, Z. & Wéber, Z., 2012. One-dimensional P-wave velocity model for the territory of Hungary from local earthquake data, *Acta Geod. Geophys. Hung.,* **47,** 344–357.

Hanks, T.C. & Kanamori, H., 1979. A moment-magnitude scale, *J. geophys. Res.,* **84,** 2348–2350.

Hardebeck, J.L. & Shearer, P.M., 2002. A new method for determining first-motion focal mechanisms, *Bull. seism. Soc. Am.,* **92,** 2264–2276.

Herrmann, R.B., 2013. Computer programs in seismology: an evolving tool for instruction and research, *Seismol. Res. Lett.,* **84,** 1081–1088.

Horváth, F., 1993. Towards a mechanical model for the formation of the Pannonian basin, *Tectonophysics,* **226,** 333–357.

Horváth, F. *et al.*, 2006. Atlas of the present-day geodynamics of the Pannonian Basin: Euroconform maps with explanatory text, *M. Geofiz.,* **47,** 133–137 (in Hungarian with English abstract).

Jost, M.L. & Herrmann, R.B., 1989. A student's guide to and review of moment tensors, *Seismol. Res. Lett.,* **60,** 37–57.

Kilényi, É., Kröll, A., Obernauer, D., Sefara, J., Steinhauser, P., Szabó, Z. & Wessely, G., 1991. Pre-tertiary basement contour map of the Carpathian basin beneath Austria, Czechoslovakia and Hungary, *Geophys. Trans.,* **36,** 15–36.

Liu, Q., Polet, J., Komatitsch, D. & Tromp, J., 2004. Spectral-element moment tensor inversions for earthquakes in southern California, *Bull. seism. Soc. Am.,* **94,** 1748–1761.

Lomax, A. & Curtis, A., 2001. Fast, probabilistic earthquake location in 3D models using oct-tree importance sampling, *Geophys. Res. Abstr.,* **3,** 955.

Lomax, A., Virieux, J., Volant, P. & Thierry-Berge, C., 2000. Probabilistic earthquake location in 3D and layered models: introduction of a Metropolis-Gibbs method and comparison with linear locations, in *Advances in Seismic Event Location,* pp. 101–134, eds Thurber, C.H. & Rabinowitz, N., Kluwer.

Mao, W.J., Panza, G.F. & Suhadolc, P., 1994. Linearized waveform inversion of local and near-regional events for source mechanism and rupturing processes, *Geophys. J. Int.,* **116,** 784–798.

Neubauer, F., Ebner, F. & Wallbrecher, E. (eds), 1995. Tectonics of the Alpine–Carpathian–Pannonian Region, *Tectonophysics,* **242** (special issue), 1–182.

Panza, G.F. & Sarao, A., 2000. Monitoring volcanic and geothermal areas by full seismic moment tensor inversion: are non-double-couple components always artefacts of modelling?, *Geophys. J. Int.,* **143,** 353–364.

Pasyanos, M.E., Dreger, D.S. & Romanowicz, B., 1996. Toward real-time estimation of regional moment tensors, *Bull. seism. Soc. Am.,* **86,** 1255–1269.

Posgay, K. *et al.*, 1995. Asthenospheric structure beneath a Neogene basin in southeast Hungary, *Tectonophysics,* **252,** 467–484.

Reasenberg, P. & Oppenheimer, D., 1985. FPFIT, FPPLOT, and FPPAGE: FORTRAN computer programs for calculating and displaying earthquake fault-plane solutions. Open-File Rep, U.S. Geol. Surv., 85-739, 109 pp.

Riedesel, M.A. & Jordan, T.H., 1989. Display and assessment of seismic moment tensors, *Bull. seism. Soc. Am.,* **79,** 85–100.

Rubinstein, R.Y. & Kroese, D.P., 2008. *Simulation and the Monte Carlo Method,* John Wiley & Sons.

Saikia, C.K. & Herrmann, R.B., 1985. Application of waveform modeling to determine focal mechanisms of four 1982 Miramichi aftershocks, *Bull. seism. Soc. Am.,* **75,** 1021–1040.

Sarao, A., Panza, G.F., Privitera, E. & Cocina, O., 2001. Non-double-couple mechanisms in the seismicity preceding the 1991–1993 Etna volcano eruption, *Geophys. J. Int.,* **145,** 319–335.

Šílený, J., Panza, G.F. & Campus, P., 1992. Waveform inversion for point source moment tensor retrieval with variable hypocentral depth and structural model, *Geophys. J. Int.,* **109,** 259–274.

Sipkin, S.A., 1993. Display and assessment of earthquake focal mechanisms by vector representation, *Bull. seism. Soc. Am.,* **83,** 1871–1880.

Sokos, E. & Zahradnik, J., 2008. ISOLA a Fortran code and a Matlab GUI to perform multiple-point source inversion of seismic data, *Comput. Geosci.,* **34,** 967–977.

Stähler, S.C. & Sigloch, K., 2014. Fully probabilistic seismic source inversion—Part 1: efficient parameterisation, *Solid Earth,* **5,** 1055–1069.

Tarantola, A., 1987. *Inverse Problem Theory,* Elsevier.

Tóth, L., Mónus, P., Zsíros, T. & Kiszely, M., 2002. Seismicity in the Pannonian Region—earthquake data, *EGU Stephan Mueller Spec. Publ. Ser.,* **3,** 9–28.

Vavryčuk, V. & Kühn, D., 2012. Moment tensor inversion of waveforms: A two-step time-frequency approach, *Geophys. J. Int.,* **190,** 1761–1776.

Wéber, Z., 2002. Imaging Pn velocities beneath the Pannonian basin, *Phys. Earth planet. Inter.,***129,** 283–300.

Wéber, Z., 2005. Probabilistic waveform inversion for focal parameters of local earthquakes, *Acta Geod. Geophys. Hung.,* **40,** 229–239.

Wéber, Z., 2006. Probabilistic local waveform inversion for moment tensor and hypocentral location, *Geophys. J. Int.,* **165,** 607–621.

Wéber, Z., 2009. Estimating source time function and moment tensor from moment tensor rate functions by constrained L1 norm minimization, *Geophys. J. Int.,* **178,** 889–900.

Wéber, Z. & Süle, B., 2014. Source properties of the 29 January 2011 ML 4.5 Oroszlány (Hungary) mainshock and its aftershocks, *Bull. seism. Soc. Am.,* **104,** 113–127.

Wessel, P. & Smith, W.H.F., 1998. New, improved version of Generic Mapping Tools released, *EOS, Trans. Am. geophys. Un.,* **79,** 579.

Zahradnik, J. & Custódio, S., 2012. Moment tensor resolvability: application to southwest Iberia, *Bull. seism. Soc. Am.,* **102,** 1235–1254.

Zahradnik, J. & Sokos, E., 2014. The Mw 7.1 Van, Eastern Turkey, earthquake 2011: two-point source modelling by iterative deconvolution and non-negative least squares, *Geophys. J. Int.,* **196,** 522–538.

Zhao, L.S. & Helmberger, D.V., 1994. Source estimation from broadband regional seismograms, *Bull. seism. Soc. Am.,* **84,** 91–104.

Zhu, L. & Helmberger, D.V., 1996. Advancement in source estimation techniques using broadband regional seismograms, *Bull. seism. Soc. Am.,* **86,** 1634–1641.

Zoback, M.L., 1992. First and second order patterns of stress in the lithosphere: the World Stress Map Project, *J. geophys. Res.,* **97,** 11703–11728.

Zsíros, T., 2000. *Seismicity and Seismic Hazard in the Carpathian Basin: Hungarian Earthquake Catalog (456-1995),* MTA FKK GGKI, Budapest (in Hungarian).

SUPPORTING INFORMATION

Additional Supporting Information may be found in the online version of this paper:

Waveform fitting for all events (http://gji.oxfordjournals.org/lookup/suppl/doi:10.1093/gji/ggv446/-/DC1).

Please note: Oxford University Press is not responsible for the content or functionality of any supporting materials supplied by the authors. Any queries (other than missing material) should be directed to the corresponding author for the paper.